

Core–Shell Zeolitic Imidazolate Framework-8@Zeolitic Imidazolate Framework-67-Derived Nitrogen-Doped Porous Carbon Confined Co₃O₄ Nanoparticle-Embedded Polyhedron for High-Performance Sodium–Air Batteries

Jiawei Ma, Yanyan Li, Fangxi Xie,* Wenwen Yin,* and Mingmei Wu*

Na–air batteries (SABs) have attracted increasing attention in recent years due to their high energy density and abundance of sodium resources. However, their application is still hindered by the lack of effective air cathodes capable of achieving stable and long cycle life. Herein, a transition metal oxide–carbon composite material in which Co₃O₄ nanoparticles (NPs) are embedded in N-doped carbon (NC) cages (NC@Co₃O₄), synthesized through a pyrolysis-oxidation strategy derived from core–shell zeolitic imidazolate framework (ZIF)-8@ZIF-67, is reported. Benefiting from

the synergistic effects between the highly active Co₃O₄ NPs and the hollow NC cages, the NC@Co₃O₄ composite exhibits outstanding bifunctional electrocatalytic performance. When employed as an air cathode in SABs, the NC@Co₃O₄ catalyst delivers a high discharge capacity of 1385 mAh g⁻¹, a low overpotential gap of 0.44 V, and an ultralong cycling stability exceeding 250 cycles (500 h). The results presented here provide valuable insights into the rational design of high-efficiency catalysts for rechargeable SABs.

1. Introduction

Nonaqueous rechargeable metal–air batteries have been regarded as promising candidates for long-distance electrical vehicles and large-scale energy-storage systems, due to their extremely high theoretical energy density and gravimetric capacity. Among them, Sodium–air batteries (SABs) have aroused growing attention owing to their low cost and abundant sodium resource.^[1–4] Furthermore, Superoxide-based SABs are highly attractive because of their extremely low-charge overpotential and high energy efficiency.^[5] However, the discharge products of SABs are extremely complex, including NaO₂,^[6] Na₂O₂,^[7] and Na₂O₂·2H₂O.^[2] The presence of peroxide products during discharging process can cause serious problems, such as increased overpotential and poor cycling stability of SABs, as they are formed via two-electron transfer process.^[8] Moreover, restricted by the gas–liquid–solid triphase reaction mechanism, the kinetics of oxygen reduction reaction (ORR) and oxygen evolution reaction (OER) are rather sluggish, resulting in high overpotential and low energy efficiency of SABs.^[9,10] In addition, both the superoxide and peroxide products are insulating and

generally accumulate on the surface of air electrodes, resulting in diminished electronic conductivity of the electrodes.^[7] Before the pores of the air cathodes are completely filled with discharge products, there is always a “sudden death” phenomenon in SABs, leading to a capacity far below the theoretical value.^[11,12] Therefore, a highly conductive and wide-open porous air cathodes with abundant and well-dispersed catalytic sites that can facilitate the reversible deposition/decomposition of discharge products is expected to overcome the aforementioned obstacles in SABs.

Significant efforts have been devoted to the development of efficient air cathodes for SABs by employing a variety of materials, such as carbonaceous materials,^[13] noble metals,^[14] or transition metals^[15] and their compounds.^[16] Among them, carbonaceous materials are preferable air cathodes due to their excellent electronic conductivity, large surface area, and porous structure. However, their OER performance is far from satisfactory and needs to be improved.^[17,18] To further improve the OER activity of carbon-based materials, solid catalysts including noble metals^[19] or transition metals and their compounds^[20,21] are usually loaded on porous carbon substrates. Noble metals including Pt,^[22] Pd,^[23] and Ru^[24] or their oxides dispersed on substrates have been used in SABs. While, due to their high affinity toward O₂, the synthesized Pd,^[23] m-RuO₂-B-reduced graphene oxide (rGO),^[25] and RuO₂^[26] cathodes are usually promoting the ORR process through the peroxide pathway. In addition, their scarcity and preciousness further hinder their application in SABs. In contrast, transition metals and their compounds with lower price and abundant sources should be even preferred for feasible practical applications. Specifically, Co-based spinel oxide Co₃O₄, which has great cyclic stability and excellent ORR/OER activities, shows great potential as the metal–air batteries’ cathode in practical application.^[27] For example, Black et al. synthesized the Co₃O₄ grown on reduced graphene oxide (Co₃O₄/rGO) and employed as part of a

J. Ma, F. Xie, W. Yin, M. Wu

School of Chemical Engineering and Technology
Sun Yat-Sen University
Zhuhai 519082, P. R. China
E-mail: xiefx5@mail.sysu.edu.cn
yinww5@mail.sysu.edu.cn
ceswmm@mail.sysu.edu.cn

Y. Li

School of Marine Science
Sun Yat-Sen University
Zhuhai 519082, P. R. China

 Supporting information for this article is available on the WWW under https://doi.org/10.1002/batt.202500248

carbon-based oxygen electrode membrane in Li-air batteries (LABs).^[28] The presence of Co_3O_4 -containing electrodes can promote the oxidation of thick Li_2O_2 deposited in LABs and thus greatly reduce the charge plateau of the batteries. Latterly, Siegal and co-workers discovered that the dissolved Co^{2+} ions in electrolyte from solid-state Co_3O_4 phase may incorporate into the discharge product Li_2O_2 in LABs to reduce the charging overpotential. Similar phenomenon was also reported in SABs.^[29] Sun et al. fabricated Co_3O_4 -decorated carbon nanotubes (CNT) by atomic layer deposition (CNT/ Co_3O_4) cathodes and found that during charging, both dissolved $\text{Co}^{2+}/\text{Co}^{3+}$ ions at the surface of Co_3O_4 can be expected to catalyze the decomposing of peroxide/superoxide and thus reduce the charging overpotential in SABs.^[2] While, restricted by the structure of the catalysts, the achievable specific capacity (800 mAh g^{-1}) and cycling performance (20 cycles with the cutoff capacity of 300 mAh g^{-1}) of CNT/ Co_3O_4 cathodes far fail to satisfy the strict performance requirements for their commercial applications. To maximize the catalytic efficiency of Co-based catalysts, the nanostructure of this class of catalysts should be optimized to expose more catalytic active sites for the deposition and decomposition of discharge products in SABs.

Zeolitic imidazolate frameworks (ZIFs), such as ZIF-67 and ZIF-8, are a novel class of porous materials with zeolite-like 3D topological structures, abundant carbon and nitrogen ligands, as well as high metal ion contents.^[30] They are expected to be good candidates as precursor templates to design various porous nanostructured metal–carbon hybrid materials. In addition, among various nanostructures, core–shell structure is competent to offer fast electron conductive pathways and favorable mechanical robustness.^[31] Inspired by these considerations, we synthesized N-doped carbon (NC)@ Co_3O_4 composites encompassing NC shell and Co_3O_4 nanoparticles (NPs) anchored on the surface of shell deriving from core–shell ZIF-8@ZIF-67.^[32] Such a unique configuration of catalysts can not only benefit the rapid electron transport and ion diffusion but also provide abundant active sites for the deposition of discharge products. Combined with the catalytic mechanism of the dissolved $\text{Co}^{2+}/\text{Co}^{3+}$ ions at the surface of Co_3O_4 , the NC@ Co_3O_4 catalyst exhibits an advanced performance in SABs. When employed as an air cathode for SABs, a high discharge capacity of 1385 mAh g^{-1} , a low overpotential gap of 0.44 V , and an outstanding cycling stability over 250 cycles (500 h) can be achieved, far exceeding the control single-component counterparts and commercial Pt/C cathodes.

2. Results and Discussion

Figure 1a illustrates the synthesis process of NC@ Co_3O_4 . In brief, the core–shell ZIF-8@ZIF-67^[33] was first synthesized by a seed epitaxial growth due to the similar topological structures and unit cell parameters of ZIF-8 and ZIF-67,^[34] which were confirmed by X-ray diffraction (XRD) (Figure S1, Supporting Information). Scanning electron microscopy (SEM) images reveal that ZIF-8, ZIF-67, and ZIF-8@ZIF-67 show well-defined rhombic dodecahedral structures with smooth surfaces and uniform size distributions (Figure S2, Supporting Information). Afterward, ZIF-8@ZIF-67

crystals experienced a carbonization process under N_2 at 800°C for 2 h to obtain NC@ CoNC .^[35] Note that the evaporation of Zn would occur at such an annealing temperature. Numerous CNTs can be obtained on the surface (Figure S3, Supporting Information), which is according well with the previous reports.^[36] The final NC@ Co_3O_4 can be obtained by the mild oxidation of NC@ CoNC in air for 1 h. In addition, bare NC and Co_3O_4 were also fabricated by using the monomer ZIF-8 and ZIF-67, respectively. Thus-obtained bare NC, Co_3O_4 , and NC@ Co_3O_4 were first subject to structural characterizations. As for the bare NC derived from ZIF-8, SEM image in Figure S4a, Supporting Information, reveals that the perfect polyhedral nanostructures with smooth surfaces. In contrast, the Co_3O_4 samples stemming from ZIF-67 display quite grainy surfaces (Figure S4b, Supporting Information). Their XRD results in Figure S6, Supporting Information, are consist with the characteristic peaks of NC and Co_3O_4 , respectively. The NC@ Co_3O_4 samples exhibit well-defined polyhedrons with textured surfaces anchored by numerous CNTs, as clearly demonstrated in Figure 1b. This distinctive morphology inherits the structural characteristics of the NC@ CoNC precursor (Figure S3, Supporting Information). Note that the NC core is situated within the hollow interiors and the Co_3O_4 NPs and CNTs anchored on the exteriors of the NC@ Co_3O_4 (Figure 1c). The highly porous nature of these polyhedrons facilitates rapid electron transport and enhanced ion diffusion kinetics.^[2] Elemental mapping images in Figure 1d confirm the homogeneous distribution of C, N, O, and Co elements throughout the NC@ Co_3O_4 matrix. Comparative transmission electron microscope (TEM) images and energy dispersive spectroscopy (EDS) elemental mappings with NC@ CoNC (Figure S5, Supporting Information) clearly demonstrate the complete oxidation of Co NPs in the NC@ Co_3O_4 (Figure 2c,d). XRD patterns of NC@ Co_3O_4 and its intermediate product of NC@ CoNC during synthesis were further collected, as shown in Figure 1e. The XRD pattern of NC@ CoNC shows sharp peaks at 44.57° , 47.78° , 51.94° , and 76.53° . Among them, the peaks at 44.57° , 51.94° , and 76.53° are corresponding to the (111), (200), and (220) facets of Co (Fm $\bar{3}$ m, JCPDS no. 15-0806). The peak at 47.78° is corresponding to the (10-11) facets of Co (P $\bar{3}$ m1, JCPDS no. 05-0727). A broad diffraction peak at 28° could be assigned to (002) plane of graphite. After oxidation, the diffraction peaks of Co become weaker, and peaks at 30.09° , 35.44° , 43.07° , 53.96° , and 62.55° can be assigned to the (220), (311), (400), (333), and (440) facets of Co_3O_4 (JCPDS no.43-1003). The XRD results provide a direct proof of phase transforming process during the formation of NC@ Co_3O_4 .

The chemical composition and bonding information of NC@ Co_3O_4 were analyzed by X-ray photoelectron spectroscopy (XPS). The survey spectrum of NC@ Co_3O_4 confirms the existence of C, N, O, and Co (Figure S7, Supporting Information). As shown in Figure 2a, the C 1s spectrum of NC@ Co_3O_4 can be deconvoluted into three bands: C–C at 284.80 eV , C–N at 285.80 eV , and O=C=O at 289.00 eV , respectively. This is consistent with those of NC (Figure S8, Supporting Information) and NC@ CoNC (Figure S10, Supporting Information), confirming the preservation of the carbon matrix structure after the oxidation process. Additionally, the N 1s spectra of NC@ Co_3O_4 (Figure 2b), NC

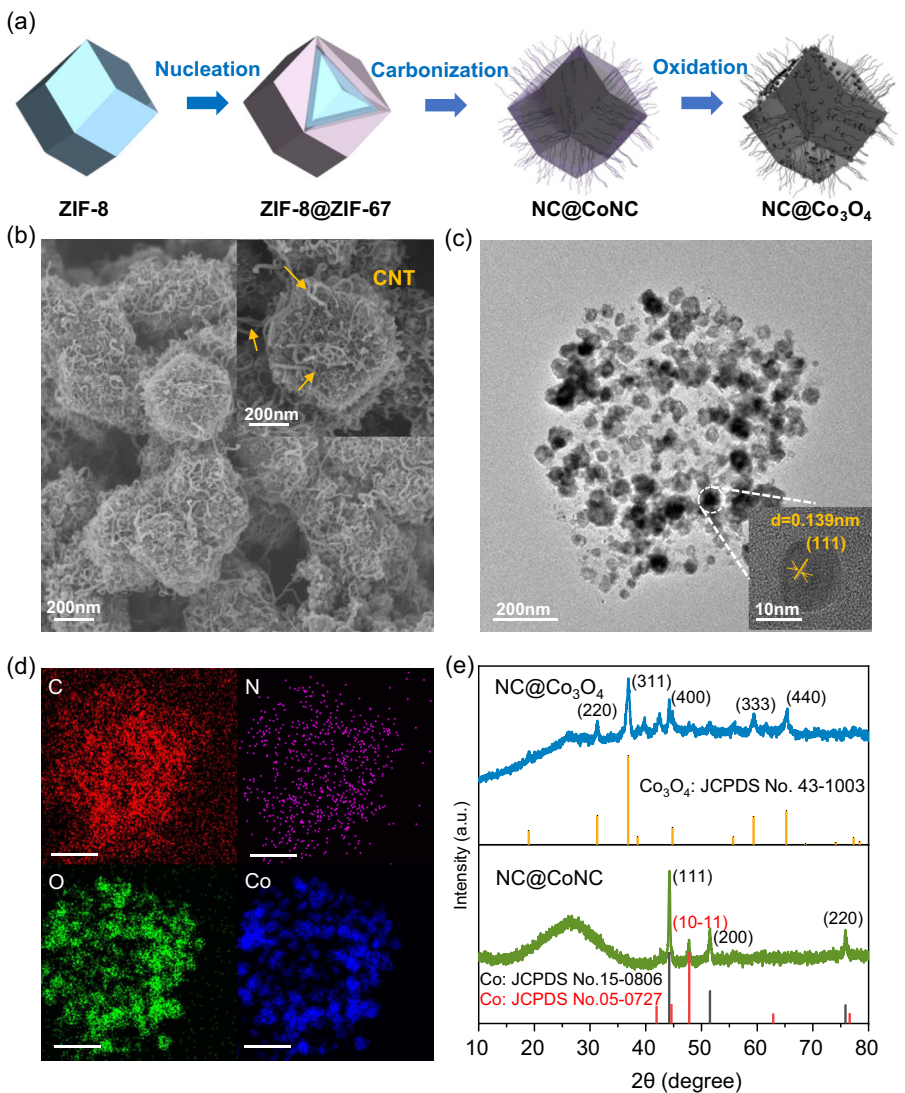


Figure 1. a) Schematic illustration of the synthetic procedure for NC@Co₃O₄. b) SEM and c) TEM and high-resolution TEM (HRTEM) images of NC@Co₃O₄. d) EDS elemental mapping images of C, N, O, and Co (the scale bar is 500 nm) of NC@Co₃O₄. e) XRD patterns of NC@CoNC and NC@Co₃O₄.

(Figure S9, Supporting Information), and NC@CoNC (Figure S11, Supporting Information) reveal the coexistence of pyridinic N (399.70 eV), pyrrolic N (398.60 eV), and graphitic N (401.50 eV) after thermal treatment. It has been reported that the pentagonal and hexagonal nitrogen centers introduced by pyrrolic N and pyridinic N, respectively, can promote high catalytic activity.^[37] The graphitic N can greatly increase the conductivity of catalysts.^[33] The nitrogen atoms doping can improve the performance of catalysts. The overall content of N in NC@Co₃O₄ reaches 5.79%. The atomic content of nitrogen species for the bare NC was measured to be 15.60% based on the XPS data (Table S1, Supporting Information). Meanwhile, the O 1s spectrum in NC@Co₃O₄ (Figure 2c) can be divided into two peaks, corresponding into C—O (531.90 eV) and Co—O (529.80 eV) peaks, respectively. The oxygen peaks indicate oxidized surface species due to exposure to the atmosphere. The XPS spectrum of Co 2p in NC@Co₃O₄ (Figure 2d) shows major peaks of Co 2p_{3/2} (780.10 eV) and Co 2p_{1/2} (795.10 eV), which further split in to subpeaks of Co³⁺ (779.90 and 794.90 eV) and Co²⁺ (781.60 and 796.70 eV). The

XPS spectrum of Co 2p in NC@Co₃O₄ reveals the absence of the metallic Co peak (778.12 eV), while this metallic peak is presented in NC@CoNC (Figure S12, Supporting Information). This observation suggests the valence states of Co ions in NC@Co₃O₄ are between +2 and +3. Raman spectrum of NC (Figure S13, Supporting Information) shows G band (1585 cm⁻¹) for sp²-hybridized carbon and D band (1340 cm⁻¹) for lattice defects. In the contrast, the spectrum of NC@Co₃O₄ (Figure 2e) exhibits a distinct peak at ≈681 cm⁻¹ which can be assigned to the doped Co-species.^[38] Moreover, the intensity ratio of D band to G band (I_D/I_G) from 1.01 (NC) to 0.903 (NC@Co₃O₄), indicating reduced defect density. Notably, NC@Co₃O₄ exhibits a further decline in I_D/I_G compared to NC@CoNC (Figure S14, Supporting Information), suggesting enhanced structural ordering due to Co₃O₄ incorporation. The presence of Co species can promote the graphitization of carbon in their vicinity during thermal decomposition and improve the electrical conductivity of the catalyst.^[36] N₂ adsorption–desorption analysis was also carried out to measure the specific surface area and pore size

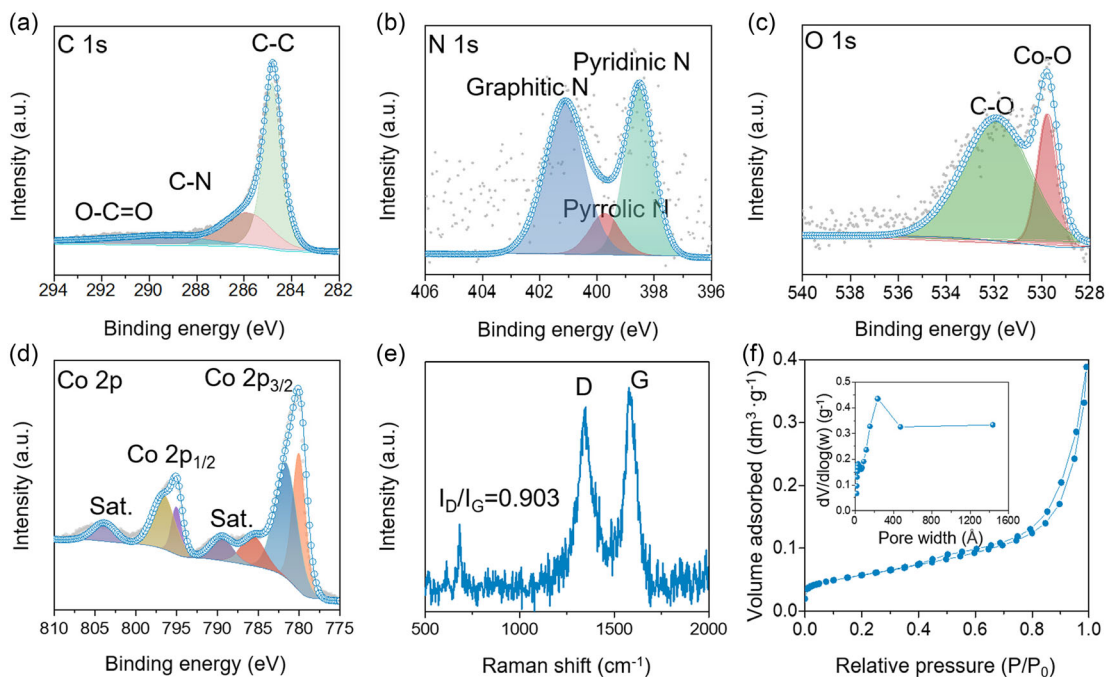


Figure 2. XPS high-resolution spectra of a) C 1s, b) N 1s, c) O 1s, and d) Co 2p in NC@Co₃O₄. e) Raman spectrum and f) N₂ adsorption–desorption isotherm (inset image: the corresponding pore size distribution) of NC@Co₃O₄.

distribution of NC@Co₃O₄ (Figure 2f). The specific surface area was measured at 204.88 m² g⁻¹, with a pore structure featuring abundant mesopores and macropores, which is beneficial to electrolyte infiltration. Compared to NC@Co₃O₄ (Figure 2f), the BET curves of NC@CoNC (Figure S15, Supporting Information) show a slight increase in pore width, indicating structural stability during oxidation.

To evaluate the electrocatalytic performance of NC@Co₃O₄, air cathodes composed of Pt/C, NC, Co₃O₄, and NC@Co₃O₄ were fabricated onto Ni foams and tested in SABs. Differential capacity (dQ/dV) analysis of initial discharge–charge profile (Figure 3a) was conducted to investigate the electrochemical catalytic activity of different cathodes. Their corresponding cathodic/anodic peak positions are listed in Figure 3b. NC and Pt/C cathodes show a single prominent cathodic peak at ≈2.05 and 2.12 V, respectively. In contrast, Co₃O₄ cathode shows a pair of redox peaks (cathodic/anodic) at 2.15/3.53 V. Especially, NC@Co₃O₄ cathode shows one cathodic peak at about 2.17 V and two anodic peaks at around 2.61/3.42 V, separately. The lower plateau around 2.61 V in the charging curve of NC@Co₃O₄ cathode is corresponding to the decomposition of Na₂O₂ in SABs. The higher plateaus at about 3.53/3.42 V in the charging curves of Co₃O₄ and NC@Co₃O₄ correspond to the decomposition of Na₂O₂ in SABs. And NC@CoNC shows a pair of redox peaks (cathodic/anodic) at 2.16 V/2.66 V, which is attributed to the decomposition of Na₂O₂ in SABs. The NC@Co₃O₄ cathode exhibits catalytic performance similar to that NC@CoNC (Figure S16a,b, Supporting Information). A more detailed analysis of these finding will be presented in the subsequent part of this study. The presence of redox peaks during the cathodic and anodic processes indicates the formation and decomposition of discharge products, respectively. The absence of an anodic peak in dQ/dV curves of NC and Pt/C catalysts

suggest that they only exhibit ORR activity in SABs. While, the Co₃O₄ catalysts can contribute to the OER of decomposing both the peroxide and superoxide products in SABs. Note that the onset potential gap between cathodic and anodic peaks of NC@Co₃O₄ is just 0.44/1.25 V, lower than that of Co₃O₄ (1.38 V). This result suggests the superior ORR and OER kinetics of the NC@Co₃O₄ cathode over the Co₃O₄ cathode in SABs. The initial discharge–charge profiles of SABs with Pt/C, NC, Co₃O₄, and NC@Co₃O₄ cathodes were investigated within a voltage range of 1.8–3.8 V at 0.05 mA cm⁻² at room temperature (Figure 3c,d). The NC@Co₃O₄ cathode shows an initial discharge capacity of 1385 mAh g⁻¹, surpassing those of Pt/C (562.92 mAh g⁻¹), NC (392.08 mAh g⁻¹), and Co₃O₄ (457.23 mAh g⁻¹). Similarly, the initial charge capacity of the NC@Co₃O₄ cathode (1051.92 mAh g⁻¹) exceeds those of Pt/C (71.75 mAh g⁻¹), NC (57.83 mAh g⁻¹), and Co₃O₄ (452.50 mAh g⁻¹) cathodes. These results indicate that NC@Co₃O₄ exhibits significantly enhanced ORR and OER activities compared to the bare NC, Co₃O₄, and commercial Pt/C cathodes. Furthermore, compared to NC@CoNC cathodes (initial discharge capacity: 846.83 mAh g⁻¹/initial charge capacity: 645.75 mAh g⁻¹, Figure S16c,d, Supporting Information), NC@Co₃O₄ cathodes also achieve an ≈60% improvement. To assess the cycling durability of these cathodes in SABs, cyclic tests were performed. To prevent overgrowth of discharge products and parasitic reactions, cyclic tests were conducted with a fixed capacity of 0.05 mAh at 0.05 mA cm⁻² (Figure 3e). The large fluctuations in the battery performance during cycling are attributed to temperature variations occurring between morning and night. NC@Co₃O₄ cathode can operate 500 h (250 cycles) without obvious discharge and charge voltage degradation. And NC@Co₃O₄ cycling curves (Figure S17, Supporting Information) show steady redox peaks and polarized potential's change. In contrast, the batteries with Pt/C, NC, and

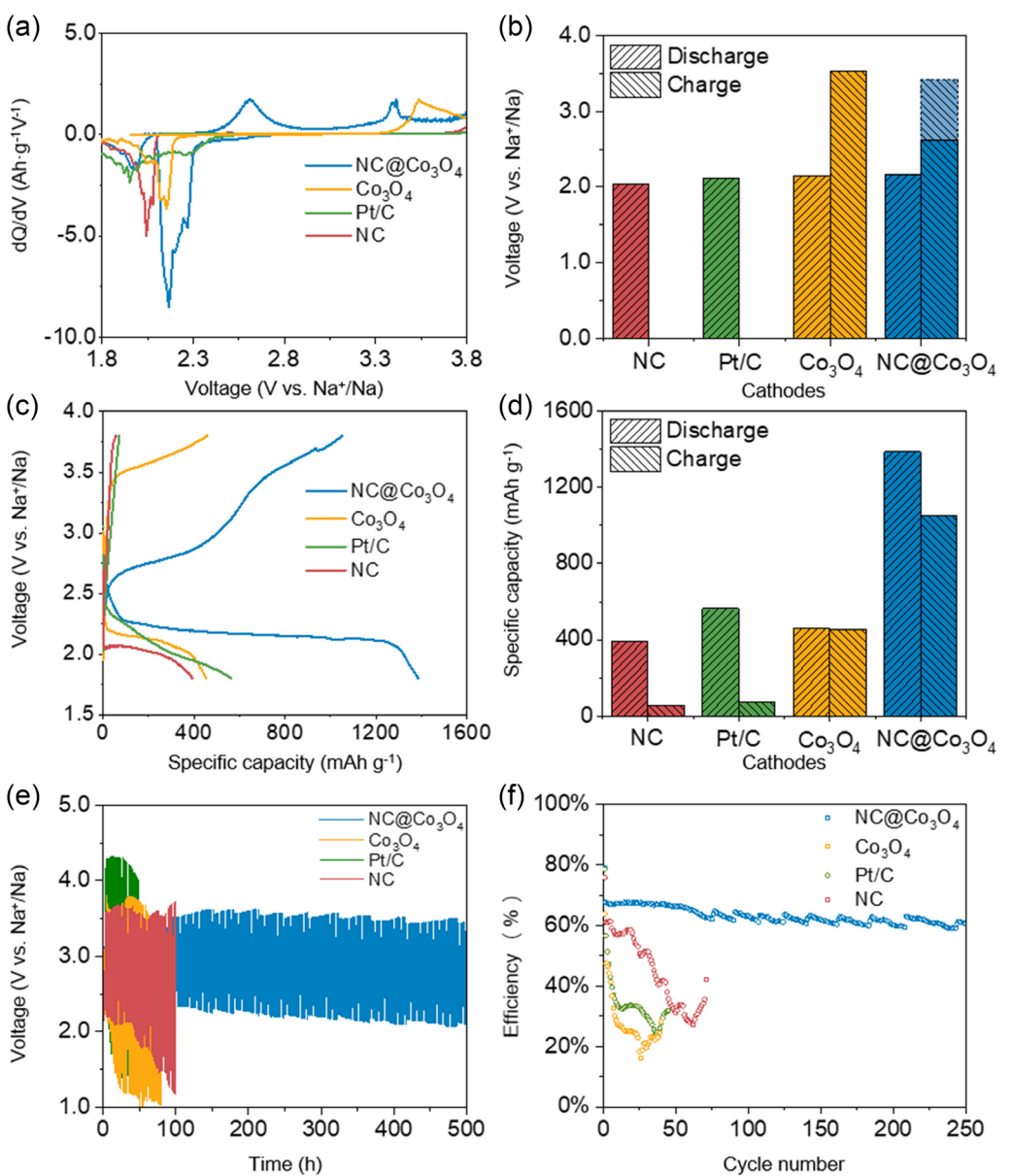


Figure 3. a) dQ/dV (differential capacity) curves of initial discharge–charge curve and b) cathodic/anodic peaks of NC, Pt/C, Co₃O₄, and NC@Co₃O₄ air cathodes in the voltage range of 1.8–3.8 V at a current density of 0.05 mA cm⁻². c) Initial discharge–charge curves and d) initial discharge/charge capacity of different cathodes at a current density of 0.05 mA cm⁻². e) Cyclic performance and f) discharge–charge efficiency of different cathodes at the current density of 0.05 mA cm⁻² with a fixed capacity of 0.05 mAh.

Co₃O₄ air cathodes can maintain operation for only 50, 100, and 80 h, respectively, and exhibited substantial discharge–charge potential drops. Additionally, as shown in Figure 3f, the discharge/charge efficiencies of NC@Co₃O₄ cathode are 70% and 60% after 250 cycles, respectively. NC@Co₃O₄ demonstrated higher efficiency compared to the bare NC, Co₃O₄, and Pt/C cathodes: NC (62%–42%, 75 cycles), Co₃O₄ (63%–28%, 40 cycles), and Pt/C (58%–30%, 50 cycles). The increased discharge capacity, narrow overpotential range, and extended cycle life of the NC@Co₃O₄ cathode compared to other materials reported previously are listed in Table S2, Supporting Information. The electrochemical performance of NC@Co₃O₄ in sodium-air batteries surpasses that of the majority of reported materials. Compared to NC@CoNC cathodes (Figure S16e,f, Supporting Information), NC@Co₃O₄ cathodes

exhibit comparable cycling durability and efficiencies. Compared to commercial Co₃O₄ cathodes (Figure S18, Supporting Information), NC@Co₃O₄ cathodes exhibit outstanding OER/ORR performance and stability.

Reversibility is important for SABs because it is necessary for them to achieve a long life span. Therefore, ex situ SEM, Raman, Fourier transform infrared spectroscopy (FTIR) were performed to clarify the composition of the initial discharge products and the air cathode after the first recharge process to measure the reversible formation and decomposition of discharge products. SEM images reveal significant differences in the surface coverage of discharge products between NC and NC@Co₃O₄ cathodes. The discharged NC cathode displayed only a few particles on its surface, demonstrating its limited ORR activity (Figure 4a). In

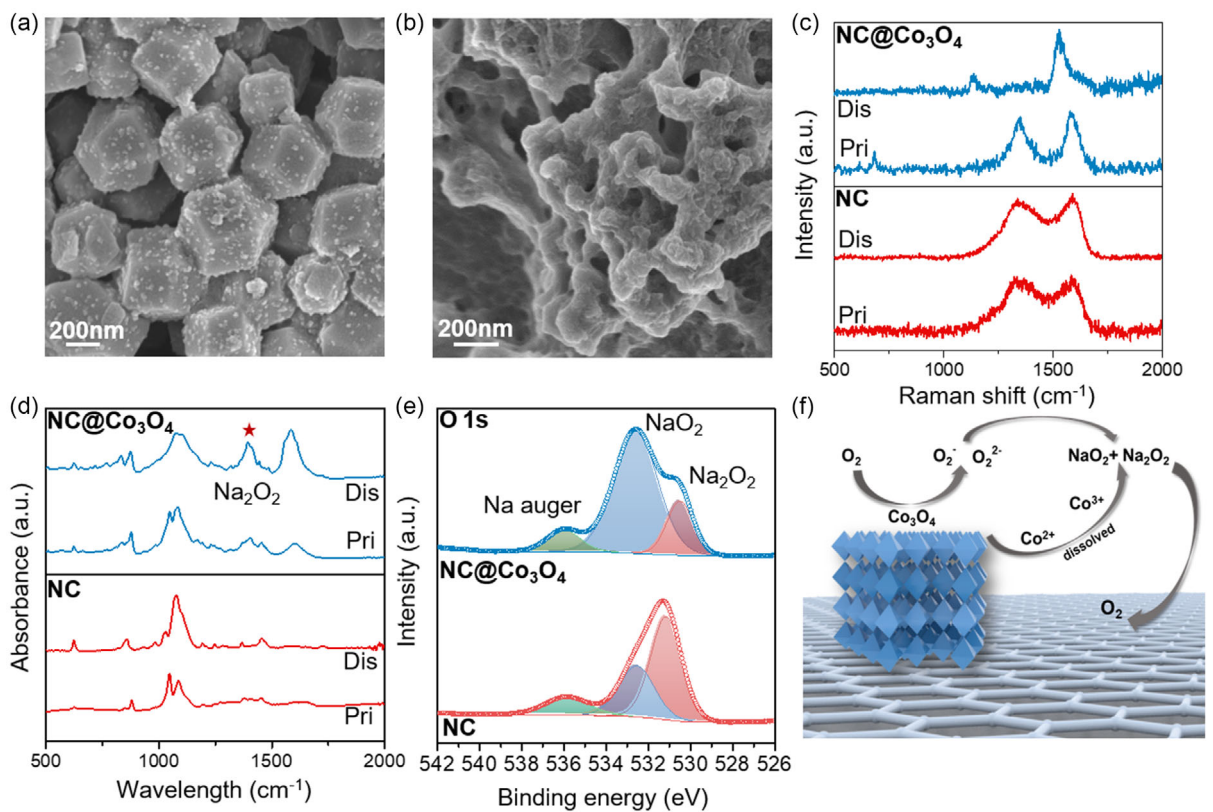


Figure 4. SEM images of a) NC and b) NC@Co₃O₄ air cathodes after the battery discharged to 1.8 V at a current density of 0.05 mA cm⁻². c) Raman spectra and d) FTIR spectra of pristine NC@CoNC cathodes (denoted as “Pri”) and NC@CoNC cathodes discharged to 1.8 V at a current density of 0.05 mA cm⁻² (denoted as “Dis”) and e) XPS spectra of O 1s of NC and NC@Co₃O₄ cathodes after the battery discharged to 1.8 V at a current density of 0.05 mA cm⁻². f) Schematic diagram of the catalyst mechanism of NC@Co₃O₄ in Na-air batteries. The dark blue octahedrons are Co₃O₄ and the light blue hexagonal cells are nitrogen-doped carbon.

contrast, the surface of the discharged NC@Co₃O₄ (Figure 4b) cathode was densely covered with granular and filmlike layers. The XRD patterns confirm the amorphous nature of the discharge products, as evidenced by the absence of characteristic diffraction peaks (Figure S19, Supporting Information). The improved surface coverage of discharge product demonstrates the significantly enhanced ORR activity of NC@Co₃O₄ cathodes. This observation is further supported by EDS elemental mapping analysis, which clearly reveals the distribution of discharge products on the cathode surface (Figure S20, Supporting Information). Notably, residual discharge products remained on the NC cathode surface after the first recharge cycle (Figure S21a, Supporting Information). In contrast, the NC@Co₃O₄ cathodes exhibited complete decomposition of discharge products (Figure S21b, Supporting Information), demonstrating comparable reversibility to the NC@CoNC cathodes (Figure S22, Supporting Information). Raman spectrum of the discharged NC cathode in Figure 4c just exhibits two characteristic D and G bands. In contrast, a peak at 1140 cm⁻¹, corresponding to NaO₂, appeared in the discharged NC@Co₃O₄ cathode, suggesting the formation of NaO₂ after the discharge process.^[39,40] Additionally, the FTIR and Raman spectra of NC@CoNC (Figure S23, Supporting Information) suggest that its discharge products have a composition similar to those of NC@Co₃O₄. This peak disappeared after recharging (Figure S24, Supporting Information),

indicating the reversibility formation and decomposition of NaO₂ in the NC@Co₃O₄ cathode. The Raman spectra exhibit significant changes occur in both D and G bands during the discharge process, with these peaks reappearing after the recharging. This reversible evolution can be attributed to the temporary deposition and the subsequent decomposition of discharge products. No Raman peak related to Na₂O₂ was detected, maybe due to its weaker Raman signal. Raman and infrared (IR) spectroscopies are complementary analytical techniques, since transitions allowed in Raman may be forbidden in IR or vice versa.^[41] As a result, the compound with weak Raman signal may show strong absorbance in IR. Accordingly, FTIR spectra of discharged cathodes were also recorded. Compared with the FTIR spectra of reference NaClO₄, Na₂O₂, Na₂CO₃ (Figure S12, Supporting Information), and pristine cathodes (Figure 4d), the FTIR spectra in Figure 4d show the presence of Na₂O₂ in all these discharged cathodes, providing evidence of Na₂O₂ (1400 cm⁻¹, Figure S25, Supporting Information) production during the discharge process. After recharging process, the peak of Na₂O₂ disappeared, indicating the decomposition of Na₂O₂ (Figure S26, Supporting Information). Note that NaO₂ does not display any characteristic peak in IR owing to the homopolar nature of the superoxide ion.^[41] XPS was employed to identify the chemical composition of the discharge products due to its high sensitivity in analytical measurements. The O 1s spectra of the discharged cathodes

(Figure 4e) display three peaks located at 531.1 eV (Na_2O_2), 532.6 eV (NaO_2), and 536.0 eV (Na auger), confirming the formation of Na_2O_2 and NaO_2 during the discharge process.^[42] Significantly, quantitative analysis of O 1s spectra reveals a substantially higher NaO_2 content (80.0%) in NC@ Co_3O_4 compared to the NC sample (37.2%). This chemical composition closely resembles that observed in NC@CoNC (Figure S27, Supporting Information), suggesting the similar surface reaction mechanisms between NC@CoNC and NC@ Co_3O_4 . The result indicates a competitive reaction between the formation of Na_2O_2 and NaO_2 during the discharge process, with the NC@ Co_3O_4 cathode favoring the formation of NaO_2 . We further examined the morphology and chemical composition of the NC and NC@ Co_3O_4 after the 5th and 15th cycles. As shown in Figure S28a,b, Supporting Information, there are still particles on the NC cathode. In the presence of NC@ Co_3O_4 cathode, the particles disappear but the filmlike discharge products appear (Figure S29a,b, Supporting Information). Corresponding O 1s spectra in Figure S28c and S29c, Supporting Information, show that the O 1s peaks of NaO_2 in NC and NC@ Co_3O_4 cathodes increase after consecutive cycles, indicating that the NaO_2 cannot completely decompose during the cycles. The presence of Na_2O_2 in the discharge products is easily covered on the surface of NaO_2 and prevents the contact of NaO_2 and catalysts, resulting in the accumulation of NaO_2 . Similar to the NC cathode, the NC@CoNC cathode demonstrates incomplete decomposition of discharge products, particularly Na_2O_2 (Figure S30, Supporting Information). This irreversible reaction accounts for the inferior cycling stability of NC@CoNC despite its comparable initial cycle efficiency to NC@ Co_3O_4 . Meanwhile, due to the dissolved $\text{Co}^{2+}/\text{Co}^{3+}$ ions at the surface of Co_3O_4 , it can effectively catalyze the decomposition of discharge products.^[43] That's the reason that there are fewer residues of discharge products in the NC@ Co_3O_4 cathodes than that of NC cathodes after continuous cycles. As is illustrated in Figure 4f, during discharging, the mixture of Na_2O_2 and NaO_2 is formed on the surface of NC@ Co_3O_4 cathodes; during charging, both dissolved $\text{Co}^{2+}/\text{Co}^{3+}$ ions at the surface of Co_3O_4 can be expected to catalyze the decomposing of peroxide/superoxide.

3. Conclusion

In this work, NC@ Co_3O_4 derived from ZIF-8@ZIF-67 has been successfully employed as a non-noble metal oxide catalyst for SABs. Compared with Pt/C, pure NC and Co_3O_4 air electrodes, the NC@ Co_3O_4 cathodes exhibit an increased capacity, decreased discharge-charge overpotential and extended cycling life in SABs due to the highly efficient utilization of well-dispersed catalytic centers and their unique configuration. The role of Co_3O_4 catalyst in SABs has been further confirmed that can promote the electrochemical decomposition of sodium peroxide and superoxide. This study demonstrates the potential of Co-based materials as an efficient catalyst for SABs. The role of catalysts in SABs is believed to be able to contribute to the future rational design for novel catalyst for these batteries.

Acknowledgements

This work was financially supported by the China Postdoctoral Science Foundation (grant no. 2021M703669), the Project of National Natural Science Foundation of China (grant no. 22405297), the Talent Recruitment Project of Guangdong (grant no. 2023QN10C330), the joint Project of National Natural Science Foundation of China (NSFC) and Guangdong Province (grant no. U1801251), and the Science and Technology Planning Project of Guangzhou City for International Cooperation Program (grant no. 201704030020).

Conflict of Interest

The authors declare no conflict of interest.

Data Availability Statement

The data that support the findings of this study are available from the corresponding author upon reasonable request.

Keywords: low-charge overpotentials • Na-air batteries • N-doped carbon (NC)@ Co_3O_4 • zeolitic imidazolate framework (ZIF)-8@ZIF-67

- [1] S. Zhao, B. Qin, K. Y. Chan, C. Y. V. Li, F. Li, *Batter. Supercaps* **2019**, *2*, 725.
- [2] Q. Sun, J. Liu, X. Li, B. Wang, H. Yadegari, A. Lushington, M. N. Banis, Y. Zhao, W. Xiao, N. Chen, J. Wang, T. K. Sham, X. Sun, *Adv. Funct. Mater.* **2017**, *27*, 1606662.
- [3] M. Salado, E. Lizundia, *Mater. Today Energy* **2022**, *28*, 101064.
- [4] X. Lin, Q. Sun, K. Doyle Davis, R. Li, X. Sun, *Carbon Energy* **2019**, *1*, 141.
- [5] H. Yadegari, X. Sun, *Trends Chem.* **2020**, *2*, 241.
- [6] X. Lin, Q. Sun, J. T. Kim, X. Li, J. Zhang, X. Sun, *Nano Energy* **2023**, *112*, 108466.
- [7] W. Yin, Z. Shadike, Y. Yang, F. Ding, L. Sang, H. Li, Z. Fu, *Chem. Commun.* **2015**, *51*, 2324.
- [8] P. Hartmann, C. L. Bender, M. Vračar, A. K. Dürr, A. Garsuch, J. Janek, P. Adelhelm, *Nat. Mater.* **2013**, *12*, 228.
- [9] Z. Zheng, J. Jiang, H. Guo, C. Li, K. Konstantinov, Q. Gu, J. Wang, *Nano Energy* **2021**, *81*, 105529.
- [10] S. Chang, M. Hou, B. Xu, F. Liang, X. Qiu, Y. Yao, T. Qu, W. Ma, B. Yang, Y. Dai, K. Chen, D. Xue, H. Zhao, X. Lin, F. Poon, Y. Lei, X. Sun, *Adv. Funct. Mater.* **2021**, *31*, 2011151.
- [11] X. Bi, R. Wang, K. Amine, J. Lu, *Small Methods* **2019**, *3*, 1800247.
- [12] W. Yin, J. Yue, M. Cao, W. Liu, J. Ding, F. Ding, L. Sang, Z. Fu, *J. Mater. Chem. A* **2015**, *3*, 19027.
- [13] C. Murugesan, B. Senthilkumar, P. Barpanda, *ACS Sustain. Chem. Eng.* **2022**, *10*, 9077.
- [14] J. Kang, W. Kwak, D. Aurbach, Y. Sun, *J. Mater. Chem. A* **2017**, *5*, 2678.
- [15] Y. Kang, S. Wang, K. S. Hui, H. F. Li, F. Liang, X. L. Wu, Q. Zhang, W. Zhou, L. Chen, F. Chen, K. N. Hui, *Mater. Today Energy* **2021**, *20*, 100572.
- [16] Y. Chen, J. Xu, P. He, Y. Qiao, S. Guo, H. Yang, H. Zhou, *Sci. Bull.* **2022**, *67*, 2449.
- [17] B. Sun, C. Pompe, S. Dongmo, J. Zhang, K. Kretschmer, D. Schröder, J. Janek, G. Wang, *Adv. Mater. Technol.* **2018**, *3*, 1800110.
- [18] W. Yin, X. Zhi, Y. Li, J. Ma, B. Johannessen, F. Xie, M. Wu, *Small* **2025**, *21*, 2500109.
- [19] Y. Zhu, F. Yang, M. Guo, L. Chen, M. Gu, *ACS Nano* **2019**, *13*, 14399.
- [20] N. Li, Y. Yin, F. Meng, Q. Zhang, J. Yan, Q. Jiang, *ACS Cat.* **2017**, *7*, 7688.
- [21] K. Xu, P. Chen, X. Li, Y. Tong, H. Ding, X. Wu, W. Chu, Z. Peng, C. Wu, Y. Xie, *J. Am. Chem. Soc.* **2015**, *137*, 4119.
- [22] T. A. Galloway, J. Dong, J. Li, G. Attard, L. J. Hardwick, *Chem. Sci.* **2019**, *10*, 2956.
- [23] L. Ma, D. Zhang, Y. Lei, Y. Yuan, T. Wu, J. Lu, K. Amine, *ACS Energy Lett.* **2018**, *3*, 276.

- [24] X. Jin, Y. Li, S. Zhang, J. Zhang, Z. Shen, C. Zhong, Z. Cai, C. Hu, H. Zhang, *Chinese Chem. Lett.* **2022**, *33*, 491.
- [25] F. Wu, Y. Xing, J. Lai, X. Zhang, Y. Ye, J. Qian, L. Li, R. Chen, *Adv. Funct. Mater.* **2017**, *27*, 1700632.
- [26] Y. Wu, X. Qiu, F. Liang, Q. Zhang, A. Koo, Y. Dai, Y. Lei, X. Sun, *Appl. Catal. B Environ. Energy* **2019**, *241*, 407.
- [27] L. Ding, T. Huang, D. Zhang, P. Qi, L. Zhang, C. Lin, H. Luo, *Electrochim. Acta* **2022**, *423*, 140577.
- [28] R. Black, J. H. Lee, B. Adams, C. A. Mims, L. F. Nazar, *Angew. Chem. Int. Ed.* **2013**, *52*, 392.
- [29] M. D. Radin, C. W. Monroe, D. J. Siegel, *Chem. Mater.* **2015**, *27*, 839.
- [30] D. Saliba, M. Ammar, M. Rammal, M. Al-Ghoul, M. Hmadedh, *J. Am. Chem. Soc.* **2018**, *140*, 1812.
- [31] C. Fu, X. Qi, L. Zhao, T. Yang, Q. Xue, Z. Zhu, P. Xiong, J. Jiang, X. An, H. Chen, J. S. Chen, A. Cabot, R. Wu, *Appl. Catal. B Environ. Energy* **2023**, *335*, 122875.
- [32] X. Yang, J. Chen, Y. Chen, P. Feng, H. Lai, J. Li, X. Luo, *Nano-Micro Lett.* **2018**, *10*, 15.
- [33] Y. Pan, K. Sun, S. Liu, X. Cao, K. Wu, W. Cheong, Z. Chen, Y. Wang, Y. Li, Y. Liu, D. Wang, Q. Peng, C. Chen, Y. Li, *J. Am. Chem. Soc.* **2018**, *140*, 2610.
- [34] J. Yang, F. Zhang, H. Lu, X. Hong, H. Jiang, Y. Wu, Y. Li, *Angew. Chem. Int. Ed.* **2015**, *54*, 10889.
- [35] P. Liu, S. Gao, Y. Wang, Y. Huang, W. He, W. Huang, J. Luo, *Chem. Eng. J.* **2020**, *381*, 122653.
- [36] Q. Sun, G. Zhu, L. Dai, W. Meng, L. Wang, S. Liu, *ACS Sustain. Chem. Eng.* **2023**, *11*, 11625.
- [37] Y. Yi, W. Zhao, Z. Zeng, C. Wei, C. Lu, Y. Shao, W. Guo, S. Dou, J. Sun, *Small* **2020**, *16*, 1906566.
- [38] Y. Li, F. Cheng, J. Zhang, Z. Chen, Q. Xu, S. Guo, *Small* **2016**, *12*, 2839.
- [39] N. Ortiz-Vitoriano, T. P. Batcho, D. G. Kwabi, B. Han, N. Pour, K. P. C. Yao, C. V. Thompson, Y. Shao-Horn, *J. Phys. Chem. Lett.* **2015**, *6*, 2636.
- [40] J. Kim, H. Lim, H. Gwon, K. Kang, *Phys. Chem. Chem. Phys.* **2013**, *15*, 3623.
- [41] H. Yadegari, Y. Li, M. N. Banis, X. Li, B. Wang, Q. Sun, R. Li, T. Sham, X. Cui, X. Sun, *Energy Environ. Sci.* **2014**, *7*, 3747.
- [42] C. Sheng, F. Yu, Y. Wu, Z. Peng, Y. Chen, *Angew. Chem. Int. Ed.* **2018**, *57*, 9906.
- [43] M. Xing, L. Kong, M. Liu, L. Liu, L. Kang, Y. Luo, *J. Mater. Chem. A* **2014**, *2*, 18435.

Manuscript received: March 31, 2025

Revised manuscript received: May 30, 2025

Version of record online:
